TMZ had recurrent tumors that were hypermutated; that is, they harbored 31.9 to 90.9 mutations per Mb (table S6). Overall, 97% of these were C>T/G>A transitions predominantly occurring at CpC and CpT dinucleotides, which is a signature of TMZ-induced mutagenesis distinct from nonhypermutated tumors (fig. S8) (*20*, *22*, *23*). We classified C>T/G>A transitions in each hypermutated tumor as TMZ-associated if they were undetected in the matched initial tumor, which was resected before TMZ treatment (Fig. 3A). Although it is difficult to definitively attribute any single mutation to TMZ exposure, comparing the C>T/G>A mutation rates in each tumor pair suggested that >98.7% are due to TMZ-induced mutagenesis (*10*). To determine whether intratumoral heterogeneity in initial tumors resulted in the misclassification of some mutations as TMZ-associated, we sequenced the exomes of three additional geographically distinct samples of the untreated initial tumor from patient 18. For mutations classified as TMZ-associated, sequencing reads with the mutation were rare in the additional exomes and were found at rates no higher than expected by chance ($1.7 \pm 0.08\%$; $P = 0.5$, Wilcoxon rank-sum test) (*10*), further suggesting that they are induced by TMZ.

Resistance to TMZ develops in part through the acquisition of mutations that inactivate the DNA mismatch repair (MMR) pathway. MMR pathway dysfunction and continued TMZ exposure can in turn result in hypermutation (*22*–*25*). Indeed, we found that hypermutated tumors acquired somatic mutations in MMR genes that were not detected in their initial tumors, as well as aberrant DNA methylation of O^6-methylguanine-DNA methyltransferase (MGMT) (fig. S3, fig. S9, and table S1).

The introduction of thousands of de novo mutations may drive the evolution of TMZ-resistant glioma cells to higher states of malignant potential (*1*, *23*). Indeed, all six recurrent tumors that showed evidence of TMZ-induced hypermutation underwent malignant progression to GBM, a high-grade tumor with a worse prognosis (*8*, *9*). To investigate this hypothesis and to identify TMZ-associated mutations that may drive the outgrowth of GBM from low-grade glioma, we focused on the RB and Akt-mTOR signaling pathways, which are associated with high-grade gliomas (Fig. 3B) (*22*, *26*–*28*). In each hypermutated recurrence, TMZ-associated mutations affected genes coding for essential signaling molecules in these two pathways. For example, in the RB pathway we identified a TMZ-associated RB1 c.2520+1G>A splice-site mutation found previously in the germ line of patients with hereditary retinoblastoma (*29*, *30*). Transcriptome sequencing confirmed that this mutation triggered aberrant splicing, premature termination, and loss of the RB1 C-terminal domain necessary for growth suppression (Fig. 3C) (*31*). Recurrent tumors from patients 05 and 10 each had a TMZ-associated *CDKN2A* $Pro^{114} \rightarrow$ Leu mutation, which prevents $p16^{INK4A}$ protein encoded by this gene from inhibiting CDK4 or inducing cell cycle arrest (*32*). The same mutation has been reported in other tumor types (*33*) and in the germ line of patients with familial melanoma (*34*). Gene set enrichment analysis further confirmed the deregulation of RB1-mediated cell cycle control upon tumor recurrence (Fig. 3D), which suggests that TMZ-associated mutations compromise the function of the RB tumor suppressor pathway.

We also investigated TMZ-associated mutations that may activate the Akt-mTOR signaling pathway. We identified a TMZ-associated mutation (*PIK3CA* $Glu^{542} \rightarrow$ Lys) in the recurrent tumor of patient 18 that drives Akt hyperactivation and induces mTOR-dependent oncogenic transformation (*35*). Similarly, the TMZ-treated second recurrence of patient 24 had TMZ-associated mutations in *PTEN* ($Ala^{121} \rightarrow$ Thr and $Gly^{165} \rightarrow$ Arg) at residues critical to its phosphatase activity (*36*) that are recurrently mutated in GBM (*33*). Finally, we validated in vitro that a TMZ-associated *MTOR* S2215F ($Ser^{2215} \rightarrow$ Phe) mutation in the recurrent tumor of patient 01 was constitutively

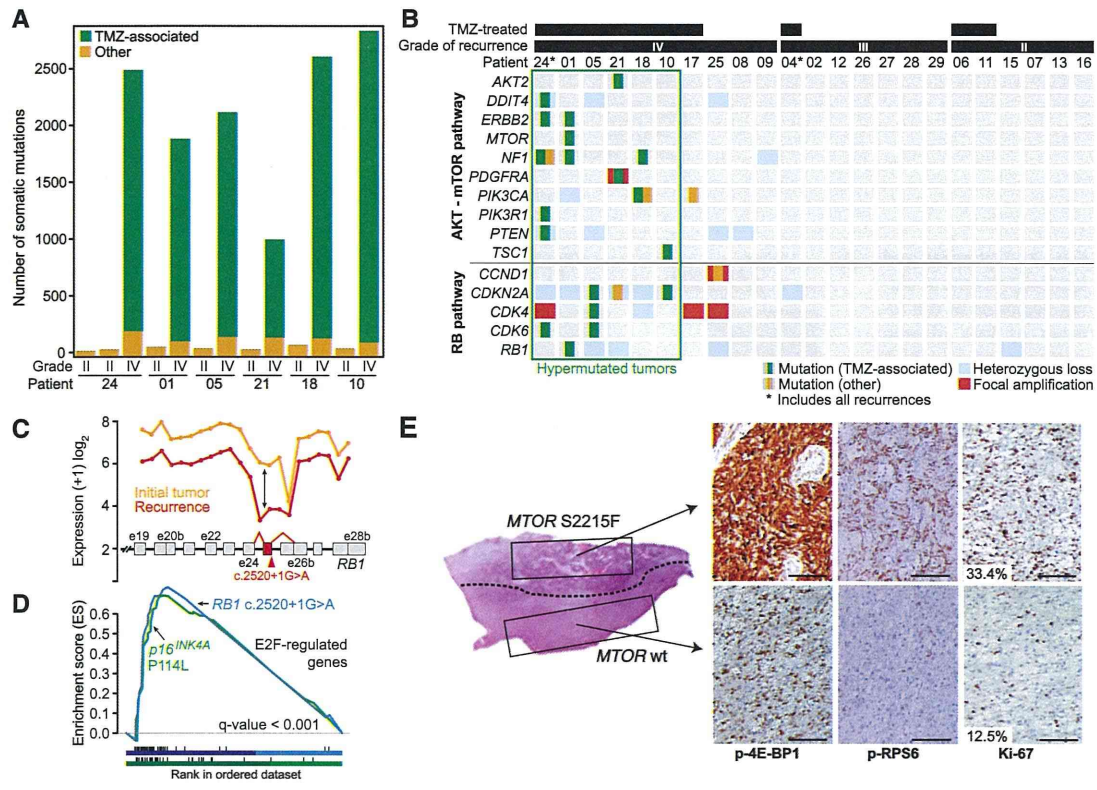

Fig. 3. Recurrent tumors from patients treated with TMZ harbor genetic alterations in the RB and Akt-mTOR signaling pathways. (**A**) Numbers of TMZ-associated mutations and other mutations identified in the six patients with hypermutated recurrent tumors. (**B**) Somatic mutations and CNAs acquired upon recurrence in key genes of pathways associated with GBM. (**C**) Expression level of *RB1* at each exon and exon-exon junction in the initial and recurrent tumor of patient 01 showing aberrant splicing of the *RB1* transcript in the recurrent tumor harboring the *RB1* c.2520+1G>A splice-site mutation. The *RB1* exon and exon junctions with significant differential usage (red) and the location of the splice-site mutation are shown. (**D**) Gene set enrichment analysis shows significant enrichment of genes down-regulated by *RB1* and up-regulated by *E2F* in the recurrent tumors of patients 01 (blue) and 10 (green), coincident with the acquisition of TMZ-associated mutations in the RB pathway. (**E**) Hematoxylin and eosin (H&E)–stained tumor sample from the first recurrent tumor of patient 01. A dotted line separates the two morphologically distinct regions. Immunohistochemistry (IHC) for phospho-RPS6, phospho-4E-BP1, and Ki-67 shows differential activation of mTORC1 targets and proliferation rates in the two adjacent regions. Scale bars, 100 μm.

activating (fig. S10), similar to the previously identified *MTOR* $Ser^{2215} \rightarrow$ Tyr (*37*). Moreover, adjacent regions of this recurrence showed heterogeneous mTOR complex 1 (mTORC1) activity (Fig. 3E and fig. S11). Microdissection revealed that although these adjacent regions shared a subset of the mutations found in the initial tumor, *MTOR* S2215F and other TMZ-associated mutations were present only in the region that stained strongly for mTORC1 activation, which also had higher staining of the proliferation marker Ki-67, implying that the TMZ-associated mutations conferred a proliferative advantage. A distal second recurrence harbored the same TMZ-associated mutations and stained strongly and homogeneously for mTORC1 targets (fig. S12). Although both regions of the first recurrence were GBM, the hypermutated subclone underwent in vivo selection, invaded distally, and seeded the second recurrence (figs. S13 and S14). Across our cohort, Akt-mTOR pathway mutations corresponded with elevated phospho-4E-BP1 and RPS6 in vivo, indicating hyperactivated mTORC1 in recurrent GBMs relative to their initial tumors (fig. S12).

There was no evidence that the mutations in the RB and Akt-mTOR signaling pathways preceded TMZ treatment, according to analysis of additional geographically distinct samples of initial tumors from four of the six patients with hypermutated recurrent tumors (table S7). Non-hypermutated recurrent tumors that progressed to GBM also acquired genetic changes in these signaling pathways, but through alternative mechanisms. In contrast, none of the grade II-III recurrences acquired mutations in these pathways. These data suggest a connection among TMZ treatment, driver mutations in oncogenic signaling pathways, and malignant progression.

Through direct comparison of the genomic landscape of gliomas at initial diagnosis and recurrence, we were able to infer the mutational character of the infiltrating tumor cells that give rise to recurrence and that adjuvant therapy with TMZ is intended to eliminate. Recurrences did not typically arise from cells bearing the full set of mutations found in the initial tumor, as would be expected from a local recurrence in the absence of selective pressure from adjuvant chemotherapy. This finding complicates the use of tumor genomics to design precision therapies targeting residual disease. We also demonstrated an alternative evolutionary path of low-grade glioma that is largely determined by adjuvant chemotherapy with TMZ. This extends earlier studies of primary GBMs (*23*, *25*), unpaired recurrent tumors (*22*), and a cell culture model (*20*). Future basic and clinical studies must weigh the initial antitumor effects of TMZ against the potential risk of inducing new driver mutations and malignant progression. Ultimately, a better understanding of the invading cells that give rise to recurrent tumors and the effect of adjuvant therapeutics on their evolution will facilitate the development of new strategies to delay or prevent recurrence and malignant progression.

References and Notes

1. M. Gerlinger, C. Swanton, *Br. J. Cancer* **103**, 1139–1143 (2010).
2. M. Greaves, C. C. Maley, *Nature* **481**, 306–313 (2012).
3. D. A. Landau *et al.*, *Cell* **152**, 714–726 (2013).
4. L. Ding *et al.*, *Nature* **481**, 506–510 (2012).
5. M. Gerlinger *et al.*, *N. Engl. J. Med.* **366**, 883–892 (2012).
6. S. Yachida *et al.*, *Nature* **467**, 1114–1117 (2010).
7. X. Wu *et al.*, *Nature* **482**, 529–533 (2012).
8. N. Sanai, S. Chang, M. S. Berger, *J. Neurosurg.* **115**, 948–965 (2011).
9. M. Westphal, K. Lamszus, *Nat. Rev. Neurosci.* **12**, 495–508 (2011).
10. See supplementary materials on *Science* Online.
11. Y. Jiao *et al.*, *Oncotarget* **3**, 709–722 (2012).
12. T. Watanabe, S. Nobusawa, P. Kleihues, H. Ohgaki, *Am. J. Pathol.* **174**, 1149–1153 (2009).
13. K. Watanabe *et al.*, *Clin. Cancer Res.* **3**, 523–530 (1997).
14. P. P. Medina *et al.*, *Hum. Mutat.* **29**, 617–622 (2008).
15. S. Glaros, G. M. Cirrincione, A. Palanca, D. Metzger, D. Reisman, *Cancer Res.* **68**, 3689–3696 (2008).
16. D. Rohle *et al.*, *Science* **340**, 626–630 (2013).
17. N. J. Szerlip *et al.*, *Proc. Natl. Acad. Sci. U.S.A.* **109**, 3041–3046 (2012).
18. A. Sottoriva *et al.*, *Proc. Natl. Acad. Sci. U.S.A.* **110**, 4009–4014 (2013).
19. L. M. F. Merlo, J. W. Pepper, B. J. Reid, C. C. Maley, *Nat. Rev. Cancer* **6**, 924–935 (2006).
20. W. J. Bodell, N. W. Gaikwad, D. Miller, M. S. Berger, *Cancer Epidemiol. Biomarkers Prev.* **12**, 545–551 (2003).
21. C. Greenman *et al.*, *Nature* **446**, 153–158 (2007).
22. Cancer Genome Atlas Research Network, *Nature* **455**, 1061–1068 (2008).
23. C. Hunter *et al.*, *Cancer Res.* **66**, 3987–3991 (2006).
24. D. P. Cahill *et al.*, *Clin. Cancer Res.* **13**, 2038–2045 (2007).
25. S. Yip *et al.*, *Clin. Cancer Res.* **15**, 4622–4629 (2009).
26. G. Reifenberger, J. Reifenberger, K. Ichimura, P. S. Meltzer, V. P. Collins, *Cancer Res.* **54**, 4299–4303 (1994).
27. H. Wang *et al.*, *Lab. Invest.* **84**, 941–951 (2004).
28. D. N. Louis, *Annu. Rev. Pathol.* **1**, 97–117 (2006).
29. T. Tsai *et al.*, *Arch. Ophthalmol.* **122**, 239–248 (2004).
30. C. Houdayer *et al.*, *Hum. Mutat.* **23**, 193–202 (2004).
31. X. Q. Qin, T. Chittenden, D. M. Livingston, W. G. Kaelin Jr., *Genes Dev.* **6**, 953–964 (1992).
32. J. Koh, G. H. Enders, B. D. Dynlacht, E. Harlow, *Nature* **375**, 506–510 (1995).
33. S. A. Forbes *et al.*, *Curr. Protoc. Hum. Genet.* Chapter 10, Unit 10.11 (2008).
34. M. C. Fargnoli *et al.*, *J. Invest. Dermatol.* **111**, 1202–1206 (1998).
35. S. Kang, A. G. Bader, P. K. Vogt, *Proc. Natl. Acad. Sci. U.S.A.* **102**, 802–807 (2005).
36. S. Y. Han *et al.*, *Cancer Res.* **60**, 3147–3151 (2000).
37. T. Sato, A. Nakashima, L. Guo, K. Coffman, F. Tamanoi, *Oncogene* **29**, 2746–2752 (2010).

Acknowledgments: We thank S. Gonzalez for assistance with the collection of clinical information; R. Kang for assistance with mutation validation; H. van Thuijl for assistance with MGMT methylation; and J. Wiencke and G. Hsuang for assistance with droplet digital PCR. Supported by Accelerate Brain Cancer Cure (J.F.C.), the Grove Foundation, the TDC Foundation, the Anne and Jason Farber Foundation, the Samuel Waxman Cancer Research Foundation, the Alex Lemonade Stand Foundation, the Entertainment Industry Foundation and Anne Feeley, and a generous gift from the Dabbiere family. Also supported by National Institute of General Medical Sciences grant T32GM008568 (T.M.); NIH grants 1T32CA15102201 and R25NS070680 (M.B.); NIH grant P50CA097257 (L.E.J., S.J.N., M.S.B., S.M.C., J.F.C., and B.S.T.); National Cancer Institute grants R01CA169316-01 (J.F.C.), P01CA81403 (W.C.G., E.C., and W.A.W.), P30CA82103 (A.B.O.), and R01CA163336 (J.S.S.); National Institute of Neurological Disorders and Stroke grant K08NS079485 (W.C.G., E.C., and W.A.W.); the UCSF Academic Senate and the Sontag Foundation (J.S.S., J.F.C., and B.S.T.); the BC Cancer Foundation, Genome BC, and Genome Canada (M.A.M.); the Goldhirsh Foundation (J.F.C.); and a research program of the Project for Development of Innovative Research on Cancer Therapeutics (P-Direct) (A.M., N.S., and H.A.), Grant-in-Aid for Scientific Research on Innovative Areas (no. 23134501) (A.M.), and Grant-in-Aid for Scientific Research (S) (no. 24221011) (H.A.) from the Ministry of Education, Culture, Sports, Science and Technology of Japan. C.Y.M. was a Damon Runyon Cancer Research Postdoctoral Fellow. M.A.M. is a Canada Research Chair in Genome Science. All exome and transcriptome sequencing data have been deposited in the European Genome-phenome Archive under accession number EGAS00001000579, and data from patients 24 to 29 have also been deposited to the Japanese Genotype-phenotype Archive under accession number JGAS00000000004.

Supplementary Materials

www.sciencemag.org/content/343/6167/189/suppl/DC1
Materials and Methods
Figs. S1 to S14
Tables S1 to S7
References (*38*–*61*)

2 May 2013; accepted 27 November 2013
Published online 12 December 2013;
10.1126/science.1239947

Single-Cell RNA-Seq Reveals Dynamic, Random Monoallelic Gene Expression in Mammalian Cells

Qiaolin Deng,[1]* Daniel Ramsköld,[1,2]* Björn Reinius,[1,2] Rickard Sandberg[1,2]†

Expression from both alleles is generally observed in analyses of diploid cell populations, but studies addressing allelic expression patterns genome-wide in single cells are lacking. Here, we present global analyses of allelic expression across individual cells of mouse preimplantation embryos of mixed background (CAST/Ei × C57BL/6J). We discovered abundant (12 to 24%) monoallelic expression of autosomal genes and that expression of the two alleles occurs independently. The monoallelic expression appeared random and dynamic because there was considerable variation among closely related embryonic cells. Similar patterns of monoallelic expression were observed in mature cells. Our allelic expression analysis also demonstrates the de novo inactivation of the paternal X chromosome. We conclude that independent and stochastic allelic transcription generates abundant random monoallelic expression in the mammalian cell.

In diploid organisms, the zygote inherits one set of autosomal chromosomes from each parent. Although it is widely believed that transcription of autosomal genes occurs from both parental alleles, specific classes of genes have been shown to express only one, randomly

www.sciencemag.org/cgi/content/full/science.1239947/DC1

Supplementary Materials for

Mutational Analysis Reveals the Origin and Therapy-Driven Evolution of Recurrent Glioma

Brett E. Johnson, Tali Mazor, Chibo Hong, Michael Barnes, Koki Aihara, Cory Y. McLean, Shaun D. Fouse, Shogo Yamamoto, Hiroki Ueda, Kenji Tatsuno, Saurabh Asthana, Llewellyn E. Jalbert, Sarah J. Nelson, Andrew W. Bollen, W. Clay Gustafson, Elise Charron, William A. Weiss, Ivan V. Smirnov, Jun S. Song, Adam B. Olshen, Soonmee Cha, Yongjun Zhao, Richard A. Moore, Andrew J. Mungall, Steven J. M. Jones, Martin Hirst, Marco A. Marra, Nobuhito Saito, Hiroyuki Aburatani, Akitake Mukasa, Mitchel S. Berger, Susan M. Chang, Barry S. Taylor,* Joseph F. Costello*

*Corresponding author. E-mail: jcostello@cc.ucsf.edu (J.F.C.); barry.taylor@ucsf.edu (B.S.T.)

Published 12 December 2013 on *Science* Express
DOI: 10.1126/science.1239947

This PDF file includes:

Materials and Methods

Figs. S1 to S14

Captions for tables S1 to S7

References

Other supplementary material for this manuscript includes the following:

Tables S1 to S7

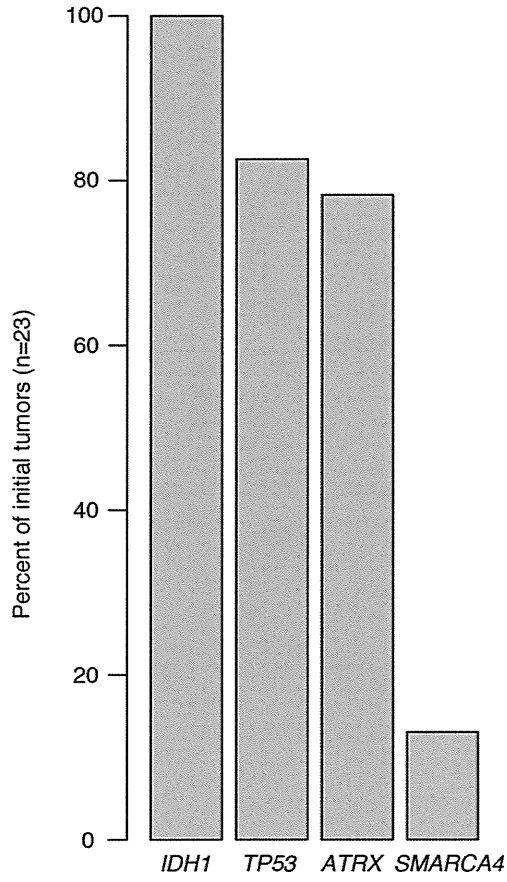

Fig. S1

Commonly mutated genes in grade II glioma. The three genes most commonly mutated in grade II glioma at initial diagnosis are each identified in >75% (23/23, 19/23, 18/23) of this cohort. The next most commonly mutated gene, *SMARCA4*, is identified in 13% (3/23) of the initial tumors in this cohort. 13 additional genes are identified in 9% (2/23) of the cohort.

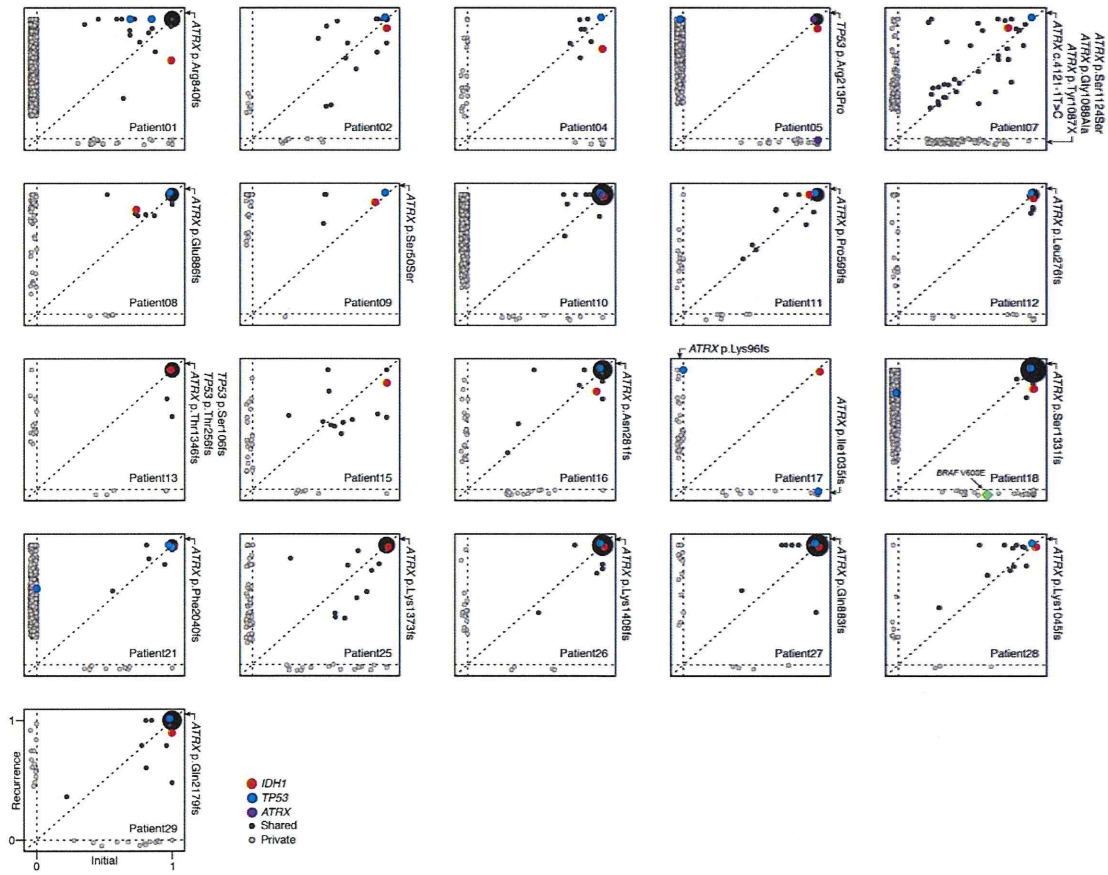

Fig. S2

Tumor cell fraction of somatic mutations in paired initial and recurrent tumors. Mutations private to tumors at initial diagnosis (x-axis), private to recurrent tumors (y-axis) or shared between the two tumors are shown as a function of the fraction of tumor cells containing the mutation. Those mutations clonal in both tumors are represented by a single point whose radius is scaled by the log count of such mutations. Key mutations are colored as indicated. Data from patients 06 and 24 were not available.

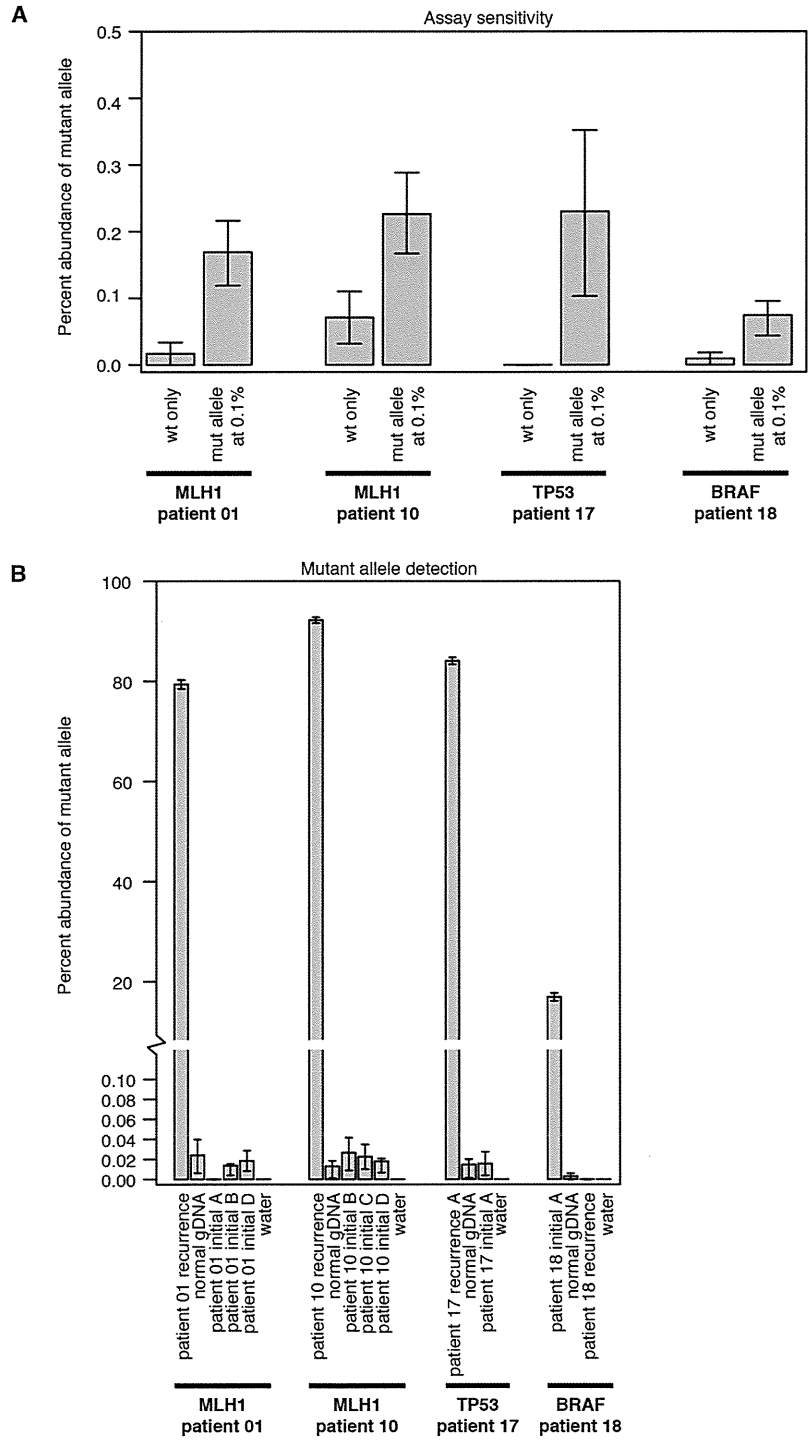

Fig. S3

Sensitive detection of mutant alleles. **(A)** Droplet digital PCR assays against 4 mutations identified as private to either an initial (BRAF in patient 18) or recurrent (MLH1 patient 01, MLH1 patient 10, TP53 patient 17) tumor can detect the mutant allele down to a

frequency of 0.1% (0.1% samples run in triplicate). The background positive level ranges from 0.01% to 0, allowing for sensitive detection of the mutant allele at 0.1%. **(B)** Geographically distinct samples of patient-matched tumor in which the mutation was not originally identified show no evidence of the mutant allele. Three distinct samples of the initial tumor from patients 01 and 10, one sample of the initial tumor from patient 17 and one sample of the recurrent tumor from patient 18 (all test samples run in quadruplicate), show background-level signals indicating that the mutant alleles are not present at a sensitivity of 0.1%. All error bars indicate the standard deviation from the Poisson calculation of allele concentrations.

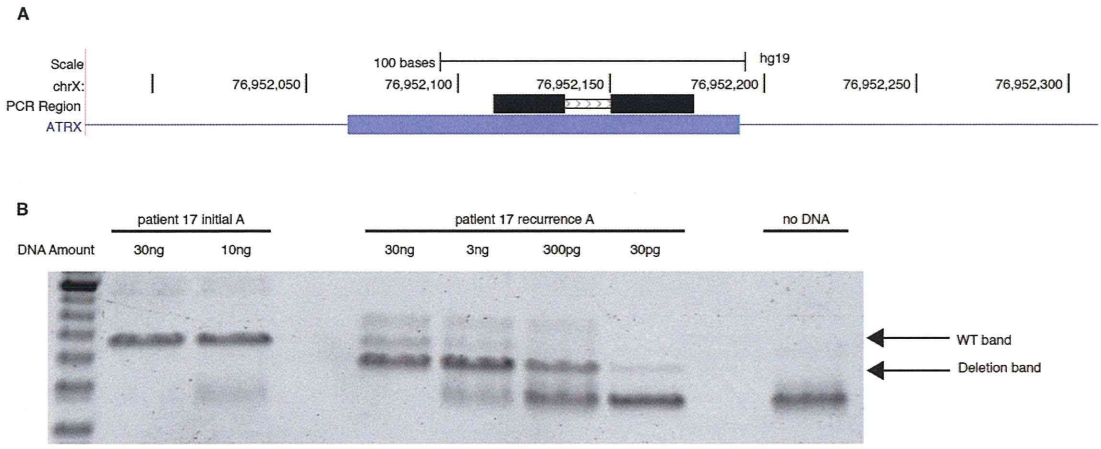

Fig. S4

Sensitive PCR analysis of an ATRX deletion in patient 17. (A) The position of the amplicon used to assess the 8bp deletion starting at chrX:76952141 identified by exome sequencing as private to the recurrence of patient 17. (B) A PCR analysis of this region using primers that flank the deletion and allow for amplification of both the wild-type (65bp) and deletion (57bp) alleles. The PCR product corresponding to the allele with a deletion was observed in patient 17 recurrent DNA with 30ng down to 30pg of template DNA. However, no such deletion-specific PCR product was observed with 30ng or 10ng of input from the initial tumor sample.

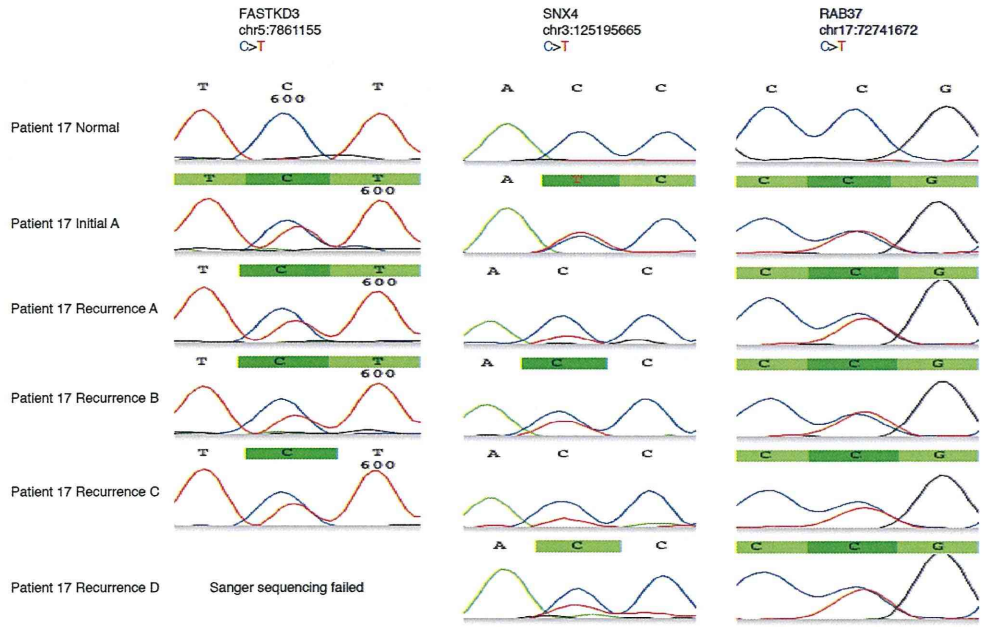

Fig. S5

Shared non-coding mutations in patient 17. Sanger sequencing confirms that at least three non-coding mutations are shared between the initial and recurrent tumors of patient 17. This indicates that these tumors diverged early in their evolutionary history from a nearest common ancestor that includes these three non-coding mutations and the shared *IDH1* R132H coding mutation.

Patient 17

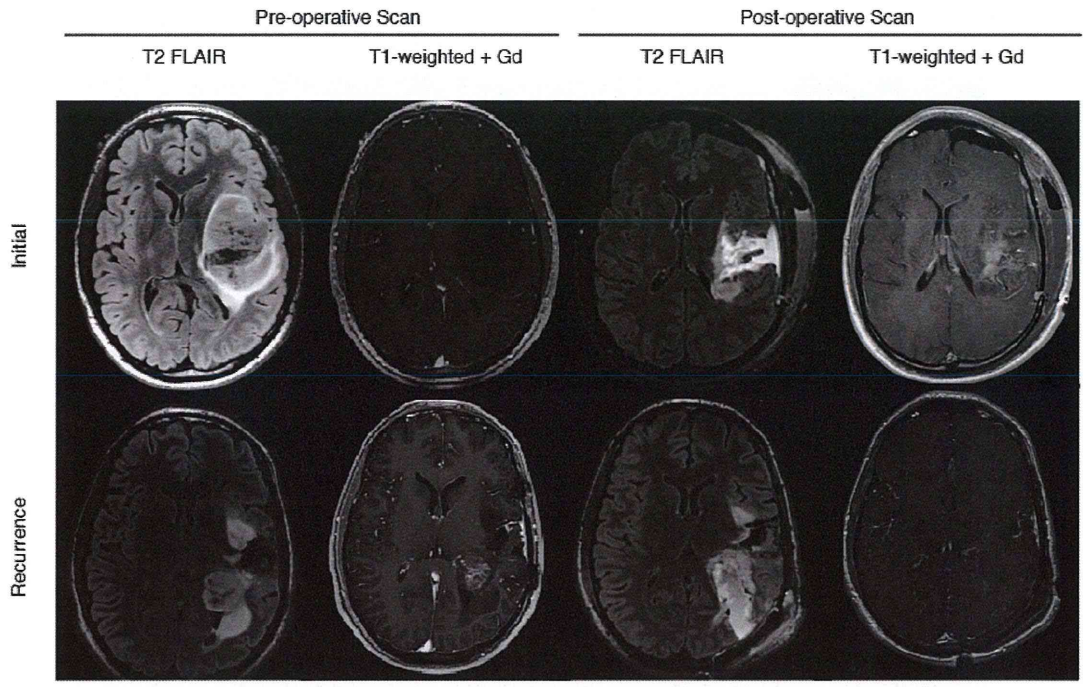

Fig. S6

Pre- and post-surgical MR imaging of patient 17. T1- and T2-weighted images representative of the tumor region before and after the initial resection and recurrence. Imaging for the initial resection demonstrated a large T2 hyperintense non-enhancing mass situated in the left insula with significant mass effect on the left lateral ventricle. After a near gross total resection the pathological diagnosis was a WHO grade II oligodendroglioma. Significant T2-hyperintensity and tissue shifts were observed post resection. At the time of recurrence, an enhancing mass centered in the left posterior temporal and parietal white matter was noted with interval growth, avid heterogeneous enhancement, and MR features consistent with upgrade to a high-grade neoplasm. Abnormal susceptibility and T1-hyperintensity with focal reduced diffusion (not shown) in the center of the mass was consistent with central necrosis. Surrounding masslike T2 hyperintensities without contrast enhancement were seen in the left insular white matter, extending into the left temporal lobe, left parietal lobe, and left corona radiata and were consistent with residual low-grade neoplasm. Gross total resection was performed on the enhancing portion of the left parietal mass and determined pathologically to be grade IV glioblastoma multiforme.

Patient 04

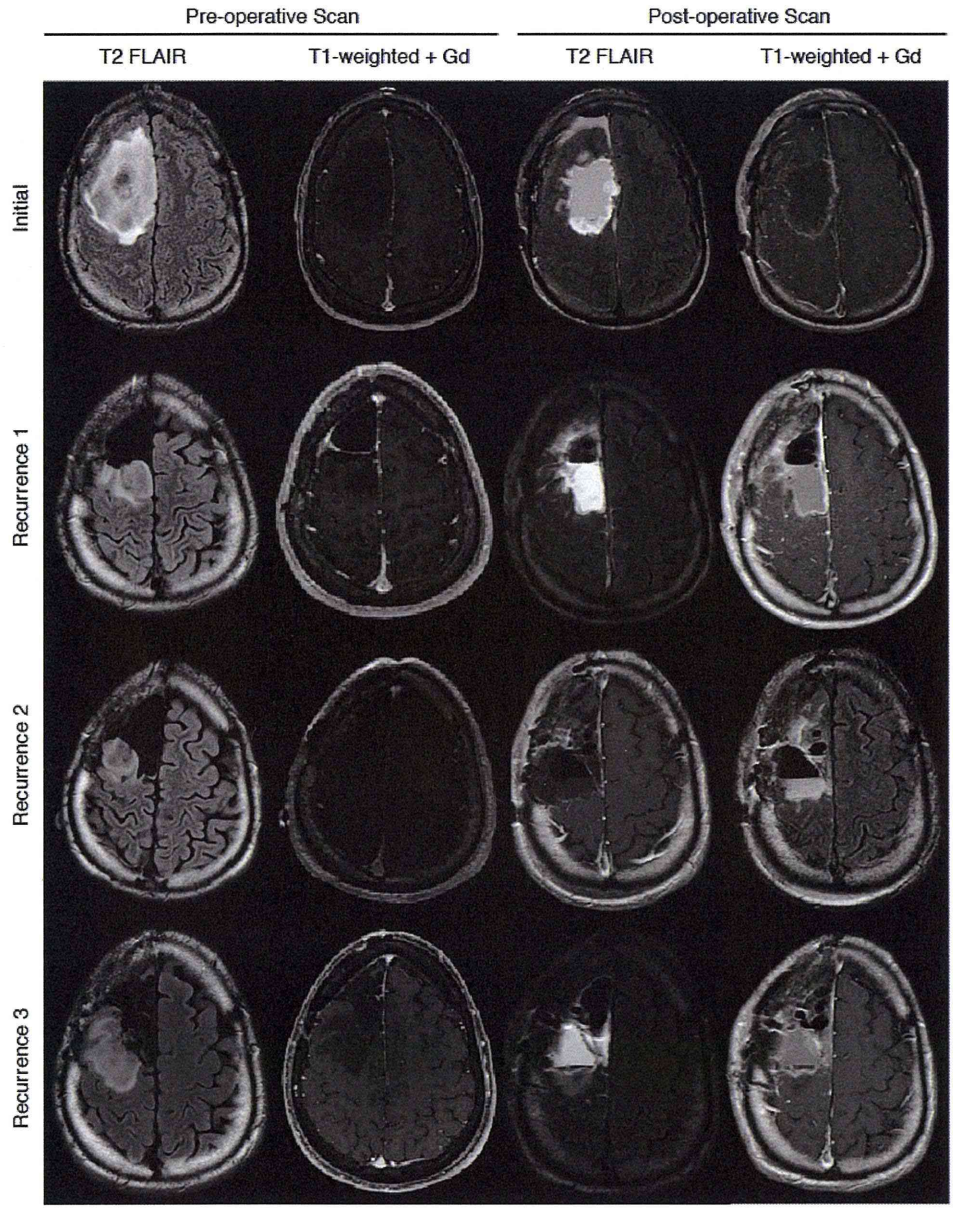

Fig. S7

Pre- and post-surgical MR imaging of patient 04. T1- and T2-weighted images representative of the tumor region before and after the initial resection and subsequent three recurrences. Imaging for the initial resection demonstrated a large T2 hyperintense non-enhancing mass situated in the right frontal lobe with significant mass effect. Perfusion imaging and spectroscopic imaging (not shown) were suggestive of low-grade neoplasm, confirmed after gross total resection to be a grade II astrocytoma. Upon first recurrence, an abnormal T2 lesion was observed along the posterior resection cavity, extending superiorly and inferiorly to the level of the lateral ventricles, with

corresponding T1 hypointensity, characteristic of highly cellular recurrent tumor. After a gross total resection, pathology analysis indicated the tumor had upgraded to a grade III anaplastic astrocytoma. At the time of the second recurrence, a mass-like non-enhancing lesion was identified in the posterior superior lateral aspect of the resection cavity with similar imaging characteristics as the previous recurrence. A gross total resection was obtained surgically, but with limited posterior margins due to proximity with the motor tracts. The lesion remained pathologically grade III. At the time of the third recurrence, there was continued interval progression of a mass-like T2 hyperintensity within the right middle frontal and precentral gyri posterior to the surgical cavity. Signal abnormality further involved the anteromedial margins of the cavity infiltrating inferiorly into the ipsilateral corona radiata. Surgical resection was limited to 80-85% due to infiltration of the motor tracts, and the tumor tissue was confirmed to remain grade III.

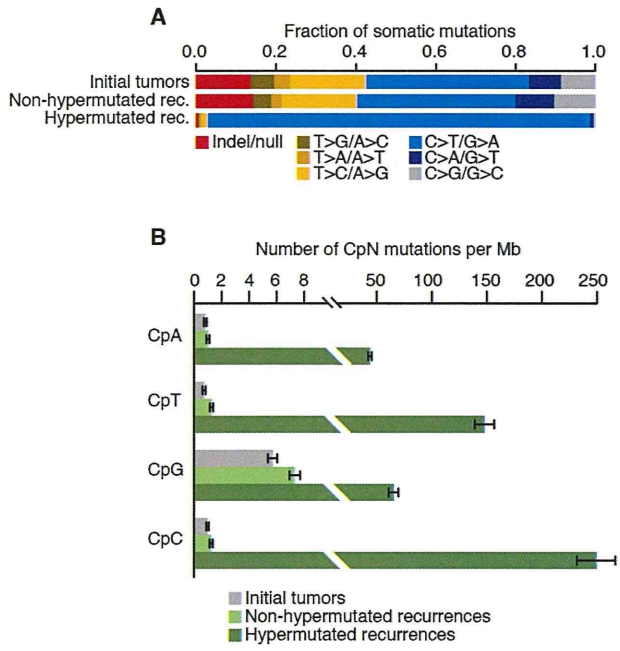

Fig. S8

The spectrum and context of somatic mutations in hypermutated and non-hypermutated gliomas. (A) The spectrum of somatic mutation types observed in initial tumors as well as both non-hypermutated and hypermutated recurrences indicates a massive increase in the C>T/G>A mutation rate in only the latter. (B) Somatic mutation rates for each CpN dinucleotide context indicates a propensity for C>T/G>A mutations to arise outside the CpG and CpA dinucleotide contexts.

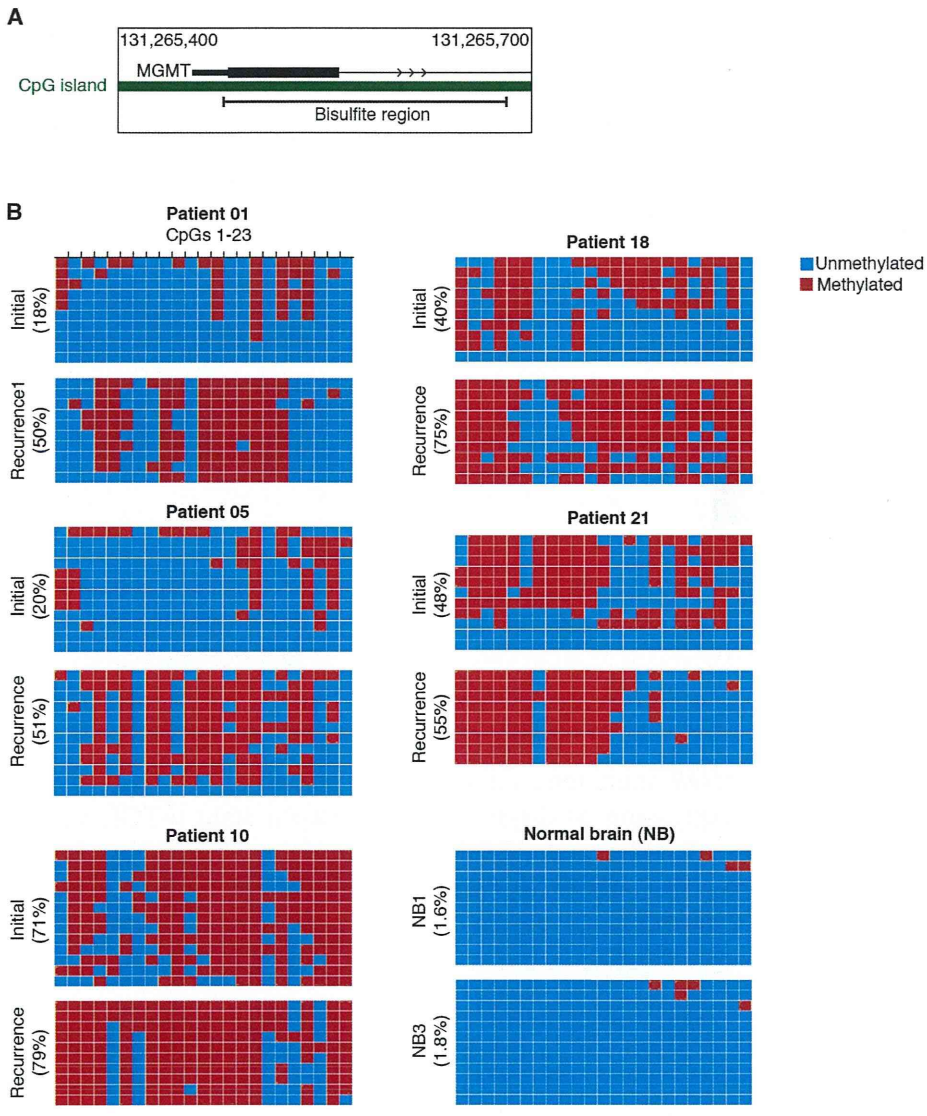

Fig. S9

The evolution of DNA methylation affecting *MGMT* during malignant progression. **(A)** The position of the amplicon used to assess *MGMT* methylation levels. **(B)** Methylation status of CpG sites in individual clones of the PCR product from bisulfite-treated DNA from the initial and recurrent tumors of patients 01, 05, 10, 18, and 21 as well as two normal brain samples. Each row represents a single clone with each CpG site marked as either methylated (red) or unmethylated (blue). The total methylation percentage of all clones is presented to the left of each panel.

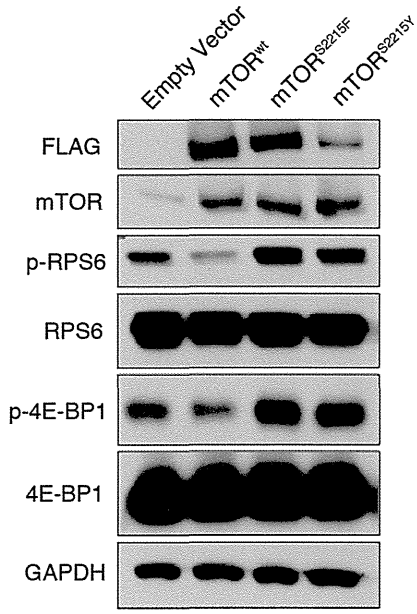

Fig. S10

Functional assessment of *MTOR* mutations on mTORC1 signaling. Western blot on protein from HEK293 cells expressing wild-type or one of two mutant mTOR vectors. Constitutive phosphorylation of RPS6 and 4E-BP1 indicates that the *MTOR* S2215F mutation constitutively activates mTORC1 signaling, much like the previously characterized *MTOR* S2215Y mutation.

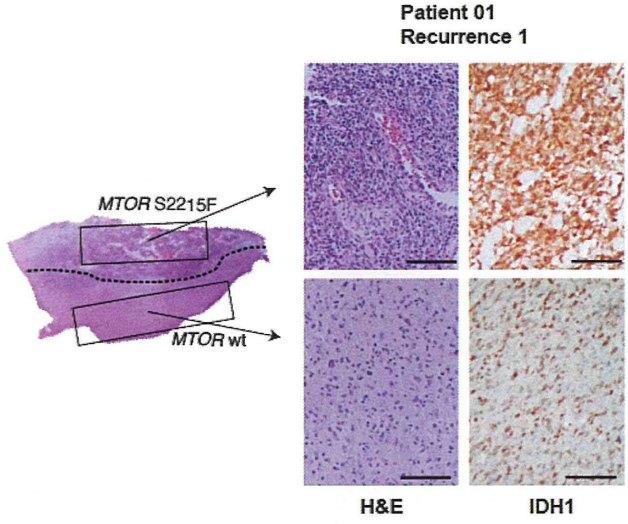

Fig. S11

Comparison of tumor samples from the first recurrence of patient 01. Hematoxylin and eosin (H&E)-stained tumor sample from the first recurrence of patient 01. A dotted line separates the two morphologically distinct regions. H&E-stained sections indicate that both regions are histologically GBM. IHC for mutant IDH1 in these same regions indicates comparable tumor content. Bars represent 100 microns.

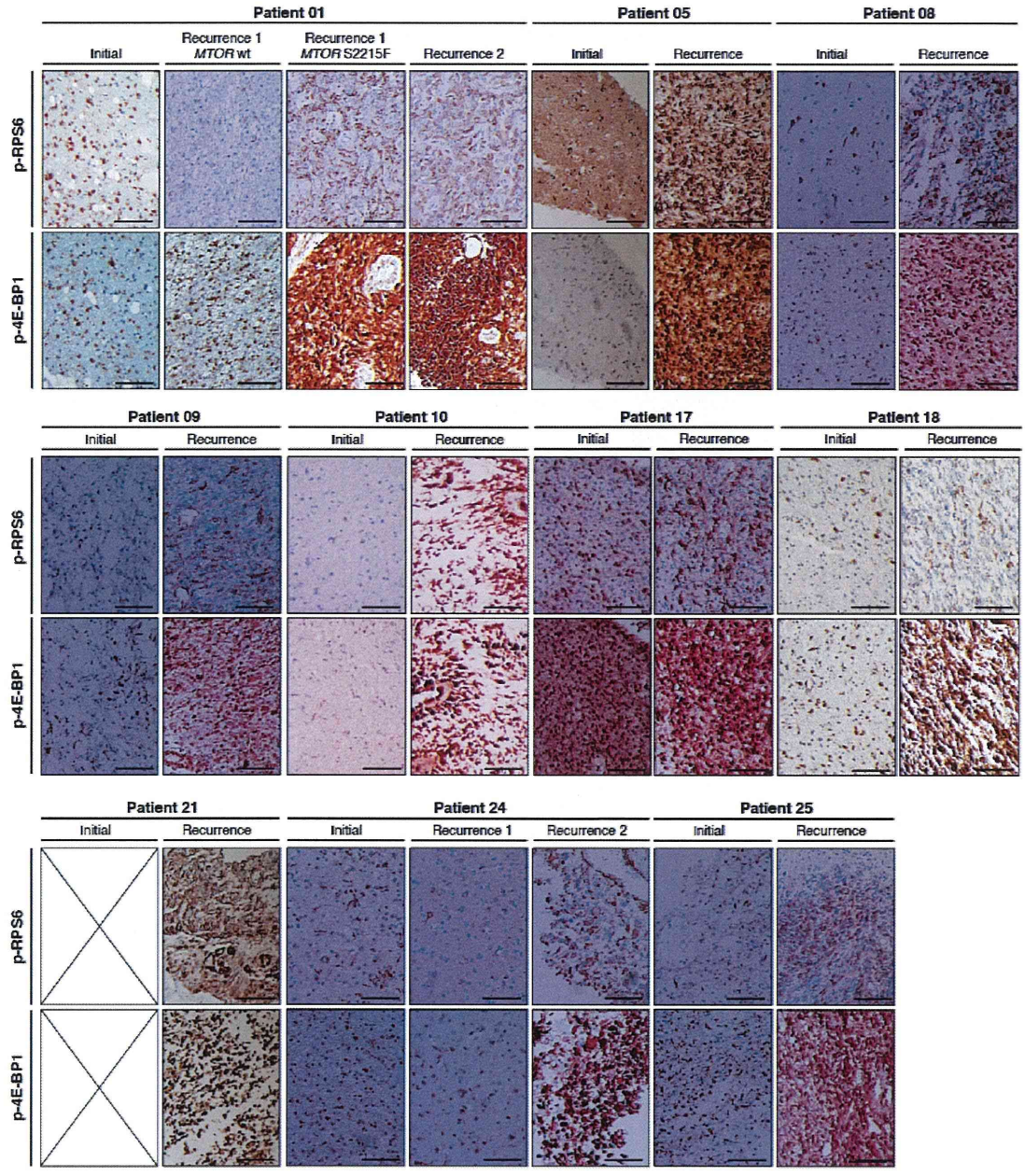

Fig. S12

mTORC1 signaling in tumors at initial diagnosis and their GBM recurrences. Immunohistochemistry (IHC) for phospho-RPS6 and phospho-4E-BP1 in the initial and recurrent tumors of all patients that undergo malignant progression to GBM indicates an increase in mTORC1 signaling across GBMs relative to the patient-matched initial tumors. Slides for the initial tumor from patient 21 were not available. Bars in all panels represent 100 microns.

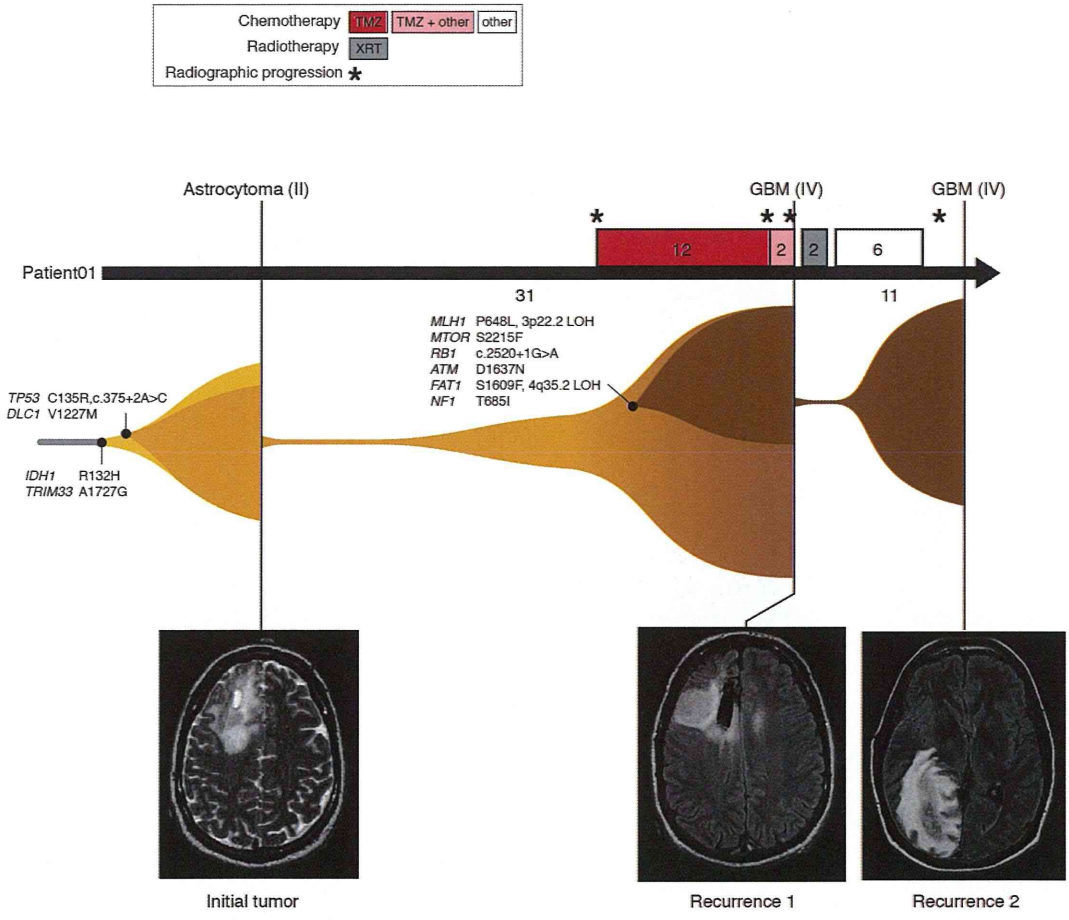

Fig. S13

An integrated timeline of the treatment, imaging, and clonal evolution of a low-grade astrocytoma that underwent TMZ-associated malignant progression. A timeline of the treatment received by patient 01 (all intervals labeled in months). Vertical bars represent tumor resections and are labeled with their diagnosis and grade (top), as well as representative MRIs (bottom). A graphical representation of one model of the clonal evolution of these tumors (middle) begins with a founding clone with early mutations in *IDH1*, *TRIM33*, *TP53* and *DLC1*. Upon first recurrence, two morphologically distinct regions of GBM are present, with only one region harboring TMZ-associated mutations in key functional cancer genes. This hypermutated clone then seeds the distal second recurrence.

Patient 01

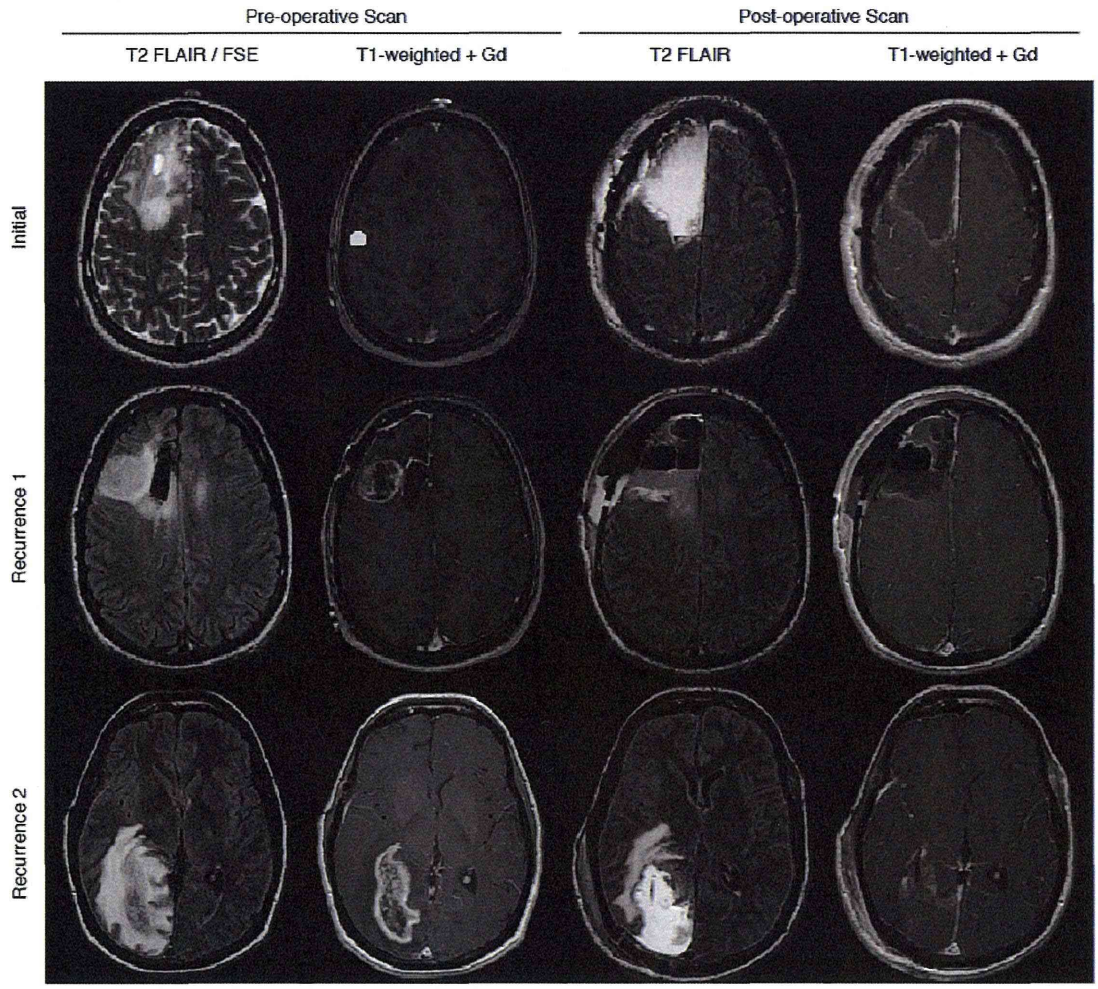

Fig. S14

Pre- and post-surgical magnetic resonance imaging of patient 01. T1- and T2-weighted images representative of the tumor region throughout the course of treatment. At the time of initial resection, the tumor lesion appeared localized to the right frontal lobe in the pre-operative scan. The first tumor recurrence was at the posterior aspect of the initial resection site, and the second recurrence was found distally in the right temporal occipital region in a lower horizontal plane. The hyper-intense region in the initial resection, pre-surgical spoiled gradient echo (SPGR), is a diffusion tensor imaging mask used for white matter tracking during surgery.

nature genetics

Recurrent mutations in multiple components of the cohesin complex in myeloid neoplasms

Ayana Kon[1], Lee-Yung Shih[2], Masashi Minamino[3], Masashi Sanada[1,4], Yuichi Shiraishi[5], Yasunobu Nagata[1], Kenichi Yoshida[1], Yusuke Okuno[1], Masashige Bando[3], Ryuichiro Nakato[3], Shumpei Ishikawa[6,7], Aiko Sato-Otsubo[1], Genta Nagae[8], Aiko Nishimoto[6], Claudia Haferlach[9], Daniel Nowak[10], Yusuke Sato[1], Tamara Alpermann[9], Masao Nagasaki[11], Teppei Shimamura[5], Hiroko Tanaka[12], Kenichi Chiba[5], Ryo Yamamoto[13], Tomoyuki Yamaguchi[13,14], Makoto Otsu[15], Naoshi Obara[16], Mamiko Sakata-Yanagimoto[16], Tsuyoshi Nakamaki[17], Ken Ishiyama[18], Florian Nolte[10], Wolf-Karsten Hofmann[10], Shuichi Miyawaki[18], Shigeru Chiba[16], Hiraku Mori[17], Hiromitsu Nakauchi[13,14], H Phillip Koeffler[19,20], Hiroyuki Aburatani[8], Torsten Haferlach[9], Katsuhiko Shirahige[3], Satoru Miyano[5,12] & Seishi Ogawa[1,4]

Cohesin is a multimeric protein complex that is involved in the cohesion of sister chromatids, post-replicative DNA repair and transcriptional regulation. Here we report recurrent mutations and deletions involving multiple components of the cohesin complex, including *STAG2*, *RAD21*, *SMC1A* and *SMC3*, in different myeloid neoplasms. These mutations and deletions were mostly mutually exclusive and occurred in 12.1% (19/157) of acute myeloid leukemia, 8.0% (18/224) of myelodysplastic syndromes, 10.2% (9/88) of chronic myelomonocytic leukemia, 6.3% (4/64) of chronic myelogenous leukemia and 1.3% (1/77) of classical myeloproliferative neoplasms. Cohesin-mutated leukemic cells showed reduced amounts of chromatin-bound cohesin components, suggesting a substantial loss of cohesin binding sites on chromatin. The growth of leukemic cell lines harboring a mutation in *RAD21* (Kasumi-1 cells) or having severely reduced expression of RAD21 and STAG2 (MOLM-13 cells) was suppressed by forced expression of wild-type RAD21 and wild-type RAD21 and STAG2, respectively. These findings suggest a role for compromised cohesin functions in myeloid leukemogenesis.

Recent genetic studies have led to the discovery of a number of new mutational targets in myeloid malignancies, unmasking unexpected roles for deregulated histone modification and DNA methylation in both acute and chronic myeloid neoplasms[1,2]. However, knowledge of the spectrum of gene mutations in myeloid neoplasms remains incomplete. We previously reported a whole-exome sequencing study of 29 paired tumor and normal samples of myeloid neoplasms with myelodysplastic features[3]. Although our major discovery was that frequent spliceosome mutations are uniquely associated with myelodysplasia phenotypes, we also identified hundreds of previously unreported gene mutations[3]. Most of those mutations affected single individuals only and are probably passenger changes. Therefore, their importance in leukemogenesis remains undetermined. However, through closer inspection of an updated list of mutations, including newly validated single-nucleotide variants, we identified additional recurrent mutations involving *STAG2*, a core component of the cohesin complex (Online Methods and **Supplementary Table 1**). In addition, we found that two other functionally related cohesin components, *STAG1* and *PDS5B*, were mutated in single specimens (**Supplementary Fig. 1**).

Cohesin is a multimeric protein complex that is conserved across species and is composed of four core subunits, SMC1, SMC3, RAD21

[1]Cancer Genomics Project, Graduate School of Medicine, The University of Tokyo, Bunkyo-ku, Tokyo, Japan. [2]Division of Hematology-Oncology, Department of Internal Medicine, Chang Gung Memorial Hospital, Chang Gung University, Taipei, Taiwan. [3]Research Center for Epigenetic Disease, Institute of Molecular and Cellular Biosciences, The University of Tokyo, Bunkyo-ku, Tokyo, Japan. [4]Department of Pathology and Tumor Biology, Graduate School of Medicine, Kyoto University, Yoshida-Konoe-cho, Kyoto-shi Sakyo-ku, Kyoto, Japan. [5]Laboratory of DNA Information Analysis, Institute of Medical Science, The University of Tokyo, Minato-ku, Tokyo, Japan. [6]Department of Pathology, The University of Tokyo, Bunkyo-ku, Tokyo, Japan. [7]Department of Genomic Pathology, Medical Research Institute, Tokyo Medical and Dental University, Bunkyo-ku, Tokyo, Japan. [8]Genome Science Division, Research Center for Advanced Science and Technology, The University of Tokyo, Meguro-ku, Tokyo, Japan. [9]Munich Leukemia Laboratory, Munich, Germany. [10]Department of Hematology and Oncology, University Hospital Mannheim, Mannheim, Germany. [11]Division of Biomedical Information Analysis, Department of Integrative Genomics, Tohoku Medical Megabank Organization, Tohoku University, Aoba-ku, Sendai, Japan. [12]Laboratory of Sequence Data Analysis, Human Genome Center, Institute of Medical Science, The University of Tokyo, Minato-ku, Tokyo, Japan. [13]Division of Stem Cell Therapy, Institute of Medical Science, The University of Tokyo, Minato-ku, Tokyo, Japan. [14]Stem Cell and Organ Regeneration Project, Exploratory Research for Advanced Technology (ERATO), Japan Science and Technology Agency (JST), Chiyoda-ku, Tokyo, Japan. [15]Stem Cell Bank, Center for Stem Cell Biology and Regenerative Medicine, Institute of Medical Science, The University of Tokyo, Minato-ku, Tokyo, Japan. [16]Department of Hematology, Faculty of Medicine, University of Tsukuba, Tsukuba, Ibaraki, Japan. [17]Division of Hematology, Department of Medicine, Showa University School of Medicine, Shinagawa-ku, Tokyo, Japan. [18]Division of Hematology, Tokyo Metropolitan Ohtsuka Hospital, Toshima-ku, Tokyo, Japan. [19]Hematology/Oncology, Cedars-Sinai Medical Center, Los Angeles, California, USA. [20]National University of Singapore, Cancer Science Institute of Singapore, Singapore. Correspondence should be addressed to S.O. (sogawa-tky@umin.ac.jp).

Received 15 February; accepted 24 July; published online 18 August 2013; doi:10.1038/ng.2731